Comparison of asymmetric and symmetric cavity configurations of erbium-doped fiber laser in active Q-switched regime

6 authors, including:

Stanislav Kolpakov
Aston University
42 PUBLICATIONS   **80** CITATIONS

SEE PROFILE

Yuri O Barmenkov
Centro de Investigaciones en Optica
153 PUBLICATIONS   **1,240** CITATIONS

SEE PROFILE

A. V. Kir'yanov
Centro de Investigaciones en Optica
248 PUBLICATIONS   **1,634** CITATIONS

SEE PROFILE

José Luis Cruz
University of Valencia
271 PUBLICATIONS   **3,070** CITATIONS

SEE PROFILE

Some of the authors of this publication are also working on these related projects:

Project   Phase array View project

Project   Frequency-shifted active Q-switching View project

Comparison of asymmetric and symmetric cavity configurations of erbium-doped fiber laser in active *Q*-switched regime

Stanislav A. Kolpakov,[1] **Yuri O. Barmenkov,**[2] **Alexander V. Kir'yanov,**[2,*] **Ana D. Guzmán-Chávez,**[3]
Jose L. Cruz,[4] and **Miguel V. Andrés**[4]

[1]*Departamento de Óptica, Universidad de Valencia, Dr. Moliner 50, 46100 Burjassot (Valencia), Spain*
[2]*Centro de Investigaciones en Óptica, Loma del Bosque 115, Col. Lomas del Campestre, 37150 Leon, Guanajuato, Mexico*
[3]*Departamento de Estudios Multidisciplinarios, División de Ingenierías, Campus Irapuato-Salamanca, Universidad de Guanajuato, Av. Universidad S/N. Col. Yacatitas, 38940 Yuriria, Guanajuato, Mexico*
[4]*Departamento de Física Aplicada—ICMUV, Universidad de Valencia, Dr. Moliner 50, 46100 Burjassot (Valencia), Spain*
*Corresponding author: kiryanov@cio.mx

We present a comparative analysis of the dynamics of an actively *Q*-switched erbium-doped fiber laser assembled in two configurations of Fabry–Pérot cavity, asymmetric and symmetric, specified by the location of an acousto-optic *Q*-switch modulator relative to the output couplers. In both configurations, the length of an active (Er^{3+}-doped) fiber is chosen such that the laser does not spuriously emit at the moments when the modulator is blocked, which is important for the pulse-on-demand operation. We show experimentally that the symmetric cavity configuration permits enlarging of the active fiber length twice as compared to the asymmetric one, thereby increasing the energy and decreasing the duration of output pulses. We also demonstrate that in the symmetric cavity configuration the laser emits a train of short (≈18 ns width on a 3 dB level) and stable *Q*-switch pulses with a couple of much smaller in magnitude adjacent subpulses. We apply the traveling waves' method for making an accurate modeling of the laser dynamics in both implementations. The modeling takes into account all the point intracavity losses as well as the distributed ones, including the loss stemming from the excited-state absorption of Er^{3+} ions. The results of numerical simulations of the laser dynamics in both implementations are shown to be in excellent agreement with experiments. © 2012 Optical Society of America

OCIS codes: 060.2410, 140.3510, 140.3540.

1. INTRODUCTION

The relative simplicity of *Q*-switched fiber lasers (QS-FLs) makes them attractive for applications in many practical areas such as laser marking and cutting [1], nonlinear frequency conversion [2,3], super-continuum generation [4–6], optical time-domain reflectometry [7], distributed fiber-optical sensing [8], light detection and ranging (LIDAR) [9], laser-initiated ignition [10], etc.

It is frequently observed in actively and passively QS-FLs with a large cavity length that output pulses have multipeak structure in the time domain where an interval between the adjacent subpeaks is approximately equal to the cavity round-trip time [11]. The traveling waves'—or the "distributed"—model, is known to explain the multipeak structure of *Q*-switch (QS) pulse's shape without any speculating on "self-mode-locking effect" to occur in a QS-FL. In contrast to the "point" model of a fiber laser, the "distributed" model accounts for both the temporal and spatial dynamics in the population inversion and powers of two contrapropagating waves in the cavity [12–14]; therefore it can address the multipeak structure of pulses even in detail, provided all the parameters of the laser system are properly accounted for [14].

Since standard fiber-coupled acousto-optical modulators (AOMs) used for *Q*-switching a QS-FL are never free from internal reflections, an active fiber should not be too long to prevent spurious lasing at the moments when an AOM is blocked

and so the active fiber is completely "charged" (i.e., inverse population reached its maximum). Otherwise it cannot effectively store energy after pumping, which limits the energy of QS pulses released. The other drawback is that a QS-FL in this case can enter one of the nonlinear dynamics regimes appearing as oscillation at subharmonics of the modulation frequency or even as chaotic oscillation [15]. The absence of spurious lasing is also a prerequisite to realize the so-called "pulse-on-demand" regime in a QS-FL or its operation at extremely low repetition rates [16].

In this paper, we discuss first how the length of active fiber (in our case, Er^{3+}-doped fiber, EDF) affects the laser operation when implementing a standard asymmetric cavity configuration where AOM is placed near one of the cavity reflectors. We show theoretically that if the EDF length increases, the QS pulses shorten and their power and energy grow. From here, one can reveal that to enhance the parameters of the QS-FL pulses, the EDF length ought to be increased. However, this length is obviously limited by a certain value that corresponds to establishing of spurious lasing; see above.

We demonstrate that a natural way to overcome this problem is the use of the symmetric configuration of the QS-FL cavity. In this case, AOM is to be placed at its center, dividing the EDF into two equal parts. The length of each piece of the EDF becomes smaller than in the asymmetric cavity configuration, which allows suppressing spurious lasing

when the fiber is completely charged. The proposed symmetric scheme of the QS-FL is, as our numerical analysis reveals, a good choice since it allows improving the QS parameters (increasing pulse energy, narrowing pulsewidth, and reducing magnitude of subpulses), due to increasing the effective EDF length twice as compared to the asymmetric configuration.

In Section 2, we formulate a background of the laser model that permits us to analyze these configurations. In this model, the traveling waves' method is applied to simulate an actively Q-switched erbium-doped fiber laser (QS-EDFL) implemented in symmetric and asymmetric Fabry–Pérot cavity configurations. Worth noticing that this is an approach that allows one to describe properly the operation of a QS-EDFL with a comparatively long cavity in the regime of short (nanosecond-range) QS pulses. In the modeling, we deal with real fiber lengths and a function that describes an AOM on/off process; moreover, we account for all the cavity losses, including the point ones at fibers' splices and other intracavity components as well as the distributed ones, e.g., the loss originated from the excited-state absorption (ESA) inherent to the EDF [17,18] and the EDF background loss.

In Section 3, we compare the results obtained numerically for these two configurations of the laser cavity, asymmetric and symmetric, and make the conclusion that the symmetric one is the most advantageous for QS-EDFLs.

In Section 4, we describe the experimental setups of QS-EDFLs assembled in asymmetric and symmetric configurations and compare the experimental results obtained with the ones obtained at the modeling. Finally, in Section 5, we formulate the conclusions and give the guidelines of how the results of the present research could be used in future practical applications.

2. THEORETICAL

A. Rate Equations

We suppose that the Er^{3+} ion is modeled by a five-level scheme [18,19] (see Fig. 1), in which each level, numbered from 1 to 5 (right side) is labeled by the energy manifold (left side). The transitions $^4I_{15/2} \rightarrow {}^4I_{11/2}$ and $^4I_{15/2} \rightarrow {}^4I_{13/2}$ designate ground-state absorption (GSA) at the pump ($\lambda_p \approx 976$ nm) and laser ($\lambda_s \approx 1550$ nm) wavelengths, respectively; the
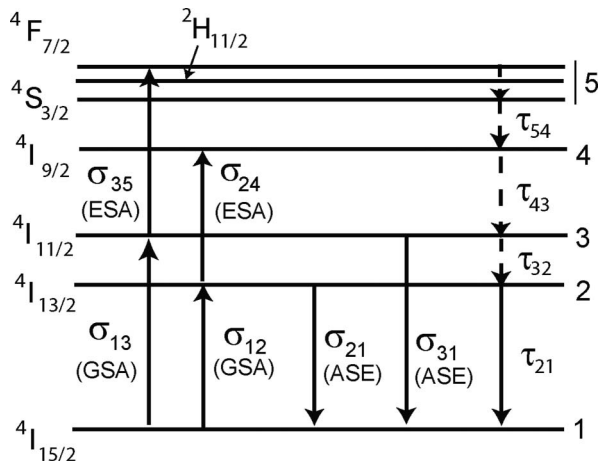

Fig. 1. Er^{3+} energy level diagram. σ_{ij} and τ_{ij} are the cross sections and decay times for the transitions connecting levels i and j.

transitions $^4I_{11/2} \rightarrow {}^4I_{15/2}$ and $^4I_{13/2} \rightarrow {}^4I_{15/2}$ designate spontaneous emission (SE) and stimulated emission at these wavelengths; and the transitions $^4I_{11/2} \rightarrow {}^4F_{7/2}$ and $^4I_{13/2} \rightarrow {}^4I_{9/2}$ designate ESA at the pump and the signal wavelengths, respectively (implying that levels "2" and "3" are populated as the result of pumping). It is also implied that level "5" comprises the three closely lying levels: $^4F_{7/2} \rightarrow {}^2H_{11/2}$, and $^4S_{3/2}$.

Notice that although the ESA processes, as inherent to the EDF [17,18], are directly accounted for in the present modeling, the cooperative up-conversion ones [20], also associated with ESA, are ignored here because we experimented with a QS-EDFL built on a standard low-doped EDF where the concentration effects are almost negligible (see below). At the same time, this assumption considerably simplifies the calculations routine.

The rate equations addressing the time evolution of populations of Er^{3+} levels are written as follows [14,18]:

$$\frac{\partial N_2}{\partial t} = \frac{\sigma_{12}^s I_s}{h\nu_s} N_1 + \frac{\sigma_{12}^{se} I_{se}}{h\nu_{se}} N_1 - \frac{\sigma_{21}^s I_s}{h\nu_s} N_2 - \frac{\sigma_{21}^{se} I_{se}}{h\nu_{se}} N_2 - \frac{\sigma_{24}^s I_s}{h\nu_s} N_2$$
$$- \frac{\sigma_{24}^{se} I_{se}}{h\nu_{se}} N_2 - \frac{N_2}{\tau_{21}} + \frac{N_3}{\tau_{32}}, \tag{1a}$$

$$\frac{\partial N_3}{\partial t} = \frac{\sigma_{13} I_p}{h\nu_p} N_1 - \frac{\sigma_{31} I_p}{h\nu_p} N_3 - \frac{N_3}{\tau_{32}} - \frac{\sigma_{35} I_p}{h\nu_p} N_3 + \frac{N_4}{\tau_{43}}, \tag{1b}$$

$$\frac{\partial N_4}{\partial t} = \frac{\sigma_{24}^s I_s}{h\nu_s} N_2 + \frac{\sigma_{24}^{se} I_{se}}{h\nu_{se}} N_2 - \frac{N_4}{\tau_{43}} + \frac{N_5}{\tau_{54}}, \tag{1c}$$

$$\frac{\partial N_5}{\partial t} = \frac{\sigma_{35} I_p}{h\nu_p} N_3 - \frac{N_5}{\tau_{54}}, \tag{1d}$$

$$N_1 + N_2 + N_3 + N_4 + N_5 = N_0, \tag{1e}$$

where $N_1 \ldots N_5$ are the populations of levels $1 \ldots 5$, which depend on time and distance along the EDF length; h is the Plank constant; ν_p, ν_s, and ν_{se} are the frequencies of the pump, signal (laser), and amplified SE (ASE) waves; σ_{ij} are the cross sections for the transitions $i \rightarrow j$ (superscripts s and se indicate that a parameter refers to a signal or SE wavelength); τ_{ij} are the relaxation times between levels i and j; I_p, I_s, and I_{se} are the pump, signal, and ASE intensities; and N_0 is the Er^{3+} ion concentration in the EDF core. The term N_2/τ_{21} in Eq. (1a) describes the number of randomly polarized SE photons emitted through a unit volume of the fiber core during a unit time, propagating in all directions.

All the intensities in Eqs. (1a)–(1e), defined as the pump, laser, and ASE powers normalized on correspondent areas of the Gaussian beams, are accepted to correspond to their values on the EDF axis. Note that though time τ_{43} is very small (≈ 5 ns; see Table 1), the population of level "4" cannot be disregarded since it is comparable with durations of subpulses adjacent to the "main" QS pulses (see below).

B. Laser Equations

Equations for the spatial-temporal evolutions of powers of the pump and two contrapropagating signal and SE waves traveling along EDF are written [14,19]:

Table 1. EDF Parameters

Parameter	Value	Units
Background (scattering) EDF loss[a]	3.1	dB/km
Low-signal absorption at 976 nm[b]	$\alpha_{p0} = 0.008$	cm^{-1}
Low-signal absorption at 1530 nm[b]	$\alpha_{se0} = 0.015$	cm^{-1}
Low-signal absorption at 1550 nm[b]	$\alpha_{s0} = 0.0069$	cm^{-1}
ESA parameter at 976 nm[c]	$\varepsilon_p = 0.95$	
ESA parameter at 1530 nm[d,e]	$\varepsilon_{se} = 0.17$	
ESA parameter at 1550 nm[d,e]	$\varepsilon_s = 0.22$	
SE/GSA cross-section ratio at 976 nm[e]	$\xi_p = 1.08$	
SE/GSA cross-section ratio at 1530 nm[d,e]	$\xi_{se} = 1.08$	
SE/GSA cross-section ratio at 1550 nm[d,e]	$\xi_s = 1.58$	
Cross section of $^4I_{15/2} \rightarrow {}^4I_{13/2}$ transition @ 1530 nm[f]	$\sigma_{12}^{se} = 5.1 \times 10^{-21}$	cm^2
Cross section of $^4I_{15/2} \rightarrow {}^4I_{13/2}$ transition @ 1550 nm[f]	$\sigma_{12}^{s} = 2.4 \times 10^{-21}$	cm^2
Cross section of $^4I_{15/2} \rightarrow {}^4I_{11/2}$ transition @ 976 nm[f]	$\sigma_{13} = 1.5 \times 10^{-21}$	cm^2
Relaxation time for $^4I_{13/2} \rightarrow {}^4I_{15/2}$ transition[b]	$\tau_{21} = 10$	ms
Relaxation time for $^4I_{11/2} \rightarrow {}^4I_{13/2}$ transition[g]	$\tau_{32} = 5.2$	μs
Relaxation time for $^4I_{9/2} \rightarrow {}^4I_{11/2}$ transition[h]	$\tau_{43} = 5$	ns
Relaxation time for $((^4F_{7/2} \rightarrow {}^2H_{11/2}/^4S_{3/2}) \rightarrow {}^4I_{9/2}$ transition[i]	$\tau_{54} = 1$	μs
Effective erbium emission linewidth[j]	$\Delta\lambda_{Er} = 60$	nm
Er^{3+} concentration in the fiber core[f]	$N_0 = 6.5 \times 10^{18}$	cm^{-3}

[a]Supplier data.
[b]Experimental data.
[c]This parameter is assumed to be equal to the one measured at 977 nm [18].
[d]Data from [17].
[e]Data from [18].
[f]Estimation made using the values of the fiber absorption, saturation powers [17,18], and the wave modal radius.
[g]Data from [18,28].
[h]Data from [21].
[i]Data from [29–31].
[j]Data from [22].

$$\left(\frac{n_p}{c}\frac{\partial}{\partial t} \pm \frac{\partial}{\partial z}\right)P_p^{\pm}(z,t) = -\alpha_p(z,t)P_p^{\pm}(z,t), \qquad (2a)$$

$$\left(\frac{n_s}{c}\frac{\partial}{\partial t} \pm \frac{\partial}{\partial z}\right)P_s^{\pm}(z,t) = g_s(z,t)P_s^{\pm}(z,t) + \frac{\Omega}{4\pi}\eta\frac{N_2(z,t)}{\tau_{21}}h\nu_s\pi a^2, \qquad (2b)$$

$$\left(\frac{n_{se}}{c}\frac{\partial}{\partial t} \pm \frac{\partial}{\partial z}\right)P_{se}^{\pm}(z,t) = g_{se}(z,t)P_{se}^{\pm}(z,t)$$
$$+ \frac{\Omega}{4\pi}(1-\eta)\frac{N_2(z,t)}{\tau_{21}}h\nu_{se}\pi a^2, \qquad (2c)$$

where n_p, n_s, and n_{se} are the modal indices for a fundamental propagation mode at the pump, laser, and SE wavelengths; c is the free-space light velocity; $P_p^{\pm}$ are the powers of the pump waves (the waves propagating to the right and left directions are labeled here and further by superscripts "+" and "–," respectively); $P_s^{\pm}$ are the powers of the two contrapropagating signal (laser) waves; $P_{se}^{\pm}$ are the powers of the two contrapropagating ASE waves; α_p is the fiber absorption at the pump wavelength ($\lambda_p \approx 976$ nm); g_s is the fiber gain at the laser wavelength ($\lambda_s = 1550$ nm, the same wavelength in the modeling and experiments); and g_{se} is the fiber gain at the SE wavelength. The second term on the right side of Eq. (2b) describes a part of SE power added to the powers of the contrapropagating laser waves on each fiber section of length dz [14,19,21]. In this term, $\Omega/4\pi$ is the portion of SE photons guided by the fiber core in each direction ($\Omega = \pi NA^2/n^2$, where NA is the fiber numerical aperture and n is the fiber clad refractive index); a is the EDF core radius; $\eta = g(\lambda_s)\Delta\lambda_s/\Delta\lambda_{Er}$ is the spectral fraction of ASE power reflected

by the fiber Bragg gratings (FBGs); $g(\lambda_s)$ is the normalized line shape at the laser wavelength [22]; $\Delta\lambda_s$ is the laser linewidth defined by the selective reflectors (FBGs); and $\Delta\lambda_{Er}$ is the effective Er^{3+} emission linewidth [22] (see Table 1). Thus, the ASE component in the model is implied to be the total emitted and amplified power within the erbium emission band while subtracting the fraction that falls to the FBG reflection band. (Notice that ASE is assigned further to have a nominal wavelength 1530 nm, even though it is actually distributed over approximately 50 nm. Such approximation allows reducing the number of differential equations and at the same time simplifying the model without losing a match between the theory and reality.)

In the asymmetric laser (Fig. 2), only one pump wave traveling to the left direction is considered. Pump absorption and signal gain within the EDF are written as follows [14]:

$$\alpha_p(z,t) = \alpha_{p0}[n_1(z,t) - (\xi_p - \varepsilon_p)n_3(z,t)] + \alpha_{BG}, \qquad (3a)$$

$$g_s(z,t) = \alpha_{s0}[(\xi_s - \varepsilon_s)n_2(z,t) - n_1(z,t)] - \alpha_{BG}, \qquad (3b)$$

$$g_{se}(z,t) = \alpha_{se0}[(\xi_{se} - \varepsilon_{se})n_2(z,t) - n_1(z,t)] - \alpha_{BG}, \qquad (3c)$$

where α_{p0}, α_{s0}, and α_{se0} are the small-signal absorption coefficients measured at the pump, laser, and SE wavelengths; α_{BG} is the fiber background (scattering) loss measured at 1200 nm (a transparence window of EDF), chosen for simplicity the same for the pump, laser, and SE wavelengths; $n_i = N_i/N_0$ are the normalized populations of Er^{3+} levels ($i = 1...5s$); $\xi_s = \sigma_{21}^s/\sigma_{12}^s$, $\xi_{se} = \sigma_{21}^{se}/\sigma_{12}^{se}$, and $\xi_p = \sigma_{31}/\sigma_{13}$; $\varepsilon_p = \sigma_{35}/\sigma_{13}$, $\varepsilon_s = \sigma_{24}^s/\sigma_{12}^s$, and $\varepsilon_{se} = \sigma_{24}^{se}/\sigma_{12}^{se}$. The lastly introduced ratios,
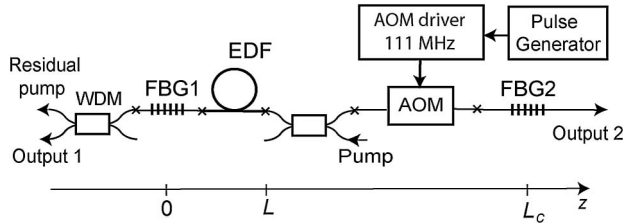
Fig. 2. Asymmetric QS configuration. WDM1 and WDM2 are 980/1550 wavelength division multiplexers; FBG1 and FBG2 are fiber Bragg gratings; crosses show the fiber splices.

specifying the EDF parameters (e.g., the ratios ε_p, ε_s, and ε_{se} define the ESA efficiency at the pump, signal, and SE wavelengths), are used for simplifying the laser equations.

A set of the rate equations [Eqs. (1a)–(1e)], the laser equations [Eqs. (2a)–(2c)], and the coupling formulas [Eqs. (3a)–(3c)], together with the formulas addressing the boundary conditions and AOM function (see below), allows one to simulate operation of the QS-EDFL with high accuracy.

C. Boundary Conditions for Asymmetric Configuration
The boundary conditions of a QS-EDFL in the asymmetric configuration (see Fig. 2) are

$$P_p(z = L, t) = P_{p0}, \tag{4a}$$

$$P_s^+(z = 0, t) = P_s^-(z = 0, t)R_1 T_1^2, \tag{4b}$$

$$P_s^-(z = L_c, t) = P_s^+(z = L_c, t)R_2 T_2^2 F_m(t)F_m(t - t_m), \tag{4c}$$

$$P_{se}^+(z = 0, t) = P_{se}^-(z = L, t) = 0, \tag{4d}$$

where P_{p0} is the pump power on the EDF input; R_1 and R_2 are the reflection coefficients of the left and right FBGs (FBG1 and FBG2), respectively; T_1 and T_2 are the transmission coefficients on all fiber splices and other laser components placed, correspondingly, between the EDF and FBG1 (T_1) and between the EDF and FBG2 (T_2); $F_m(t)$ is the AOM function [see Eq. (5) below]; t_m is the time interval corresponding to the round-trip between the AOM and FBG2 ($\approx$7.5 ns); and L_c is the cavity physical length. Notice that the transmissions of the fiber splices can be estimated using the theory presented in [23].

The laser output signals at the left-hand and right-hand outputs, P_{s1} and P_{s2}, are calculated using the following formulas:

$$P_{s1}(t) = P_s^-(z = 0, t)(1 - R_1), \tag{5a}$$

$$P_{s2}(t) = P_s^+(z = L_c, t)(1 - R_2). \tag{5b}$$

The AOM switching function obtained directly from an experiment is fitted with high precision by the following law [14]:

$$F_m(t) = \left[\begin{array}{cc} 0, & t \leq 0 \\ 0.38 \left[\frac{1}{2}\left(1 - \cos\left(\pi \frac{t}{t_r}\right)\right) \right]^{1.63}, & 0 < t < t_r \\ 0.38, & t \geq t_r \end{array} \right], \tag{6}$$

where $t_r = 50$ ns is the AOM full rise-time.

D. Boundary Conditions for Aymmetric Configuration
The boundary conditions for the QS-EDFL in the symmetrical configuration (see Fig. 3) are

$$P_p^+(z_4, t) = P_{p0}, \tag{7a}$$

$$P_p^-(z_1, t) = P_{p0}, \tag{7b}$$

$$P_s^+(0, t) = P_s^-(0, t)R_1 T_1^2, \tag{7c}$$

$$P_s^-(L_c, t) = P_s^+(L_c, t)R_2 T_2^2, \tag{7d}$$

$$P_s^+(z_4, t) = P_s^+(z_1, t)T_{12}F_m(t), \tag{7e}$$

$$P_s^-(z_1, t) = P_s^-(z_4, t)T_{12}F_m(t), \tag{7f}$$

$$P_{se}^+(0, t) = P_{se}^-(L_c, t) = 0, \tag{7g}$$

where P_{p0} is the in-core pump power at the points z_2 and z_3; R_1 and R_2 are the reflection coefficients of FBG1 and FBG2; T_1 and T_2 are the transmission coefficients of the fiber splices between the EDF1 and FBG1 (T_1) and between the EDF2 and FBG2 (T_2), respectively; T_{12} is the transmission coefficient of all fiber splices and intracavity components located between the EDF1 and EDF2; and L_c is the cavity length. The AOM length is considered in the modeling to be negligibly small. The laser output signals are calculated using Eqs. (5a) and (5b).

Note that for both laser implementations, asymmetric and symmetric, the boundary conditions for two contrapropagating signal and ASE waves are to be taken at the opposite sides of the ED-QSFL cavity. Thus, standard solving programs included into the computational languages are not applicable for the laser simulation in our case; instead, we have made our own software for numerical calculations of the developed model.

3. MODELING RESULTS

A. Asymmetric Laser Configuration
In order to obtain the dependence of the QS pulses shape on the EDF length, we solved Eqs. (1a)–(1e) and (2a)–(2c) using the traveling-wave method with the boundary conditions given by Eqs. (4a)–(4d). The EDF length was divided into a number of short equal sections with length $\Delta z = 1$ cm, on which all populations n_i were assumed to be constant through the time interval $\Delta t = \Delta z n_m / c$. For simplicity, we assumed that the modal indices for the pump, laser, and ASE wavelengths are the same and equal to $n_m = 1.45$. Repetition frequency of the QS pulses is determined by the AOM on/off repetition
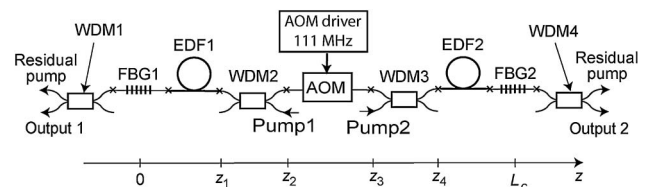

Fig. 3. Symmetric QS configuration. Pulse generator (see Fig. 2) is not shown; z_1, z_2, z_3, and z_4 indicate positions of the fiber splices (crosses).

rate that was chosen to be low enough, ensuring the initial population of the second Er^{3+} level N_2 to be at maximum. The cavity length, the gratings' reflection coefficients, the overall intracavity loss, and the EDF parameters were taken the same as in experiments (see Table 1 and Section 4). We also assumed that the reflection spectra of both FBG couplers are fully matched and that the optical spectra of QS pulses are defined by the FBGs' bandwidths.

When modeling the asymmetrical cavity configuration, the AOM was considered to be placed at one of the cavity extremes (e.g., at its right side; see Fig. 2). The EDF was considered to be pumped from the side where the AOM was placed.

At the beginning ($t = 0$), the populations of all Er^{3+} levels except level "2" (see Fig. 1) are virtually zero, whereas the second level population is nearly N_0 (in other words, pump absorption is almost null and the EDF gains for the signal and SE wavelengths are maximal). The signal waves' powers are taken equal to a small portion η of the whole ASE spectral power that is reflected by the FBG1; we assumed $\eta = 1.1 \times 10^{-3}$.

At the first step ($k = 1$, $t_1 = \Delta z n_m / c$), the AOM begins to switch on, the part η of ASE power starts to be reflected from the FBG2, and so the process of QS pulse formation begins. Then, an iterative procedure is applied: at the kth moment, the populations' distributions are found on the base of the wave powers calculated at the previous ($k - 1$)th moment. Next, the new populations are used for calculating the EDF absorption/gain profiles, which are then used, in turn, for finding new waves' powers, and so on.

Some of the results of modeling are shown in Figs. 4 and 5. In Fig. 4, snapshots of QS pulses simulated for a few EDF lengths (from 4 to 8 m) at the left-hand laser output (output 1 in Fig. 1) are demonstrated, with the cavity length being kept constant ($L_c = 10.3$ m) and with FBGs' reflections $R_1 = 0.37$ and $R_2 = 0.93$ (the values of the cavity length and FBGs' reflections that were used in experiments). It is seen that (i) each pulse contains a number of subpulses, (ii) these subpulses are separated by ≈100 ns, i.e., by the time interval

that corresponds approximately to a round-trip time through the cavity, (iii) as the EDF length becomes larger, the pulses appear earlier while the adjacent (to the "main" pulse) subpulses become smaller, and (iv) the width of the main subpulses decreases drastically with the EDF length increase (from ≈45 ns at 4 m EDF to ≈12 ns for 8 m EDF).

Figure 5(a) shows the variations of the main QS pulse power, which result from the EDF length changes. It is seen that the power generally grows with the EDF length increase, from ≈5 W (output 1) and ≈0.8 W (output 2) at 4 m fiber to ≈45 W (output 1) and 5 W (output 2) at 8 m fiber. Both dependences (obtained for the opposite outputs 1 and 2) present several specific EDF lengths at which the QS pulse power is maximal or minimal, with the most powerful peak to appear at the EDF length of ≈7.6 m. Thus, in order to maximize the laser power, one needs to choose the fiber length at which a local maximum in the output power is observed.

Figure 5(b) shows how the energy of all QS pulses is changed when varying the EDF length. The dependences for outputs 1 and 2 in this case are qualitatively similar to the ones shown in Fig. 5(a) for QS pulse power; i.e., the QS energy generally grows when increasing the EDF length. A difference between Figs. 5(a) and 5(b) is that curves 1 and 2 obtained for QS pulse energies at the opposite laser outputs demonstrate opposite ("out of phase") behaviors when increasing the EDF length [Fig. 5(b)]; that is, local pulse energy maxima at the cavity left output are observed when at its right output local minima are observed, and vice versa. In the mean time, the dependencies simulated for the QS pulse powers as a function of the EDF length are seen to be "in phase" [Fig. 5(a)]. Such behavior can be tentatively explained by nonuniform depopulation of Er^{3+} laser level at saturating the gain "seen" by a laser wave traveling along the EDF as well as by strong ESA nonlinear loss for high-power QS pulses generated [see Eq. (1c)].

The presence of extremes in the dependences shown in Fig. 5 (in particular, the presence of "optimal" EDF lengths) has a more evident explanation. At the optimal EDF length, the main subpulse, after several passes through the laser cavity, reaches the maximal power exactly at the EDF output; otherwise (if the EDF is longer than such optimal length) this subpulse loses more energy through the ESA processes and in addition it passes through the EDF, partially discharged by a previous subpulse, or (if the EDF is shorter than the optimal length) it does not seriously depopulate the Er^{3+} laser level, thereby allowing a succeeding subpulse to extract more energy from the EDF.

Notice that the EDF length is normally limited by the AOM's internal reflections. In the case where low-doped EDF and a standard fiber-coupled AOM are used (as in the experiments discussed below; see Section 4), the EDF length at which the laser doesn't yet spuriously lase at the AOM blocked is limited by approximately 4 m (the experimental value). If compared with the modeling results for the asymmetric cavity configuration presented in Fig. 5, this maximal length should limit the presence of a pure QS regime (yet without spurious CW lasing) by peak power of ≈5 W (or pulse energy of ≈1.3 μJ, at output 2). Thus, it is of a demand to properly choose another cavity geometry that would protect the laser against CW spurious lasing at the AOM blocked and at the same time to maximize the effective EDF length. The laser configuration that satisfies this demand most properly and is the simplest in
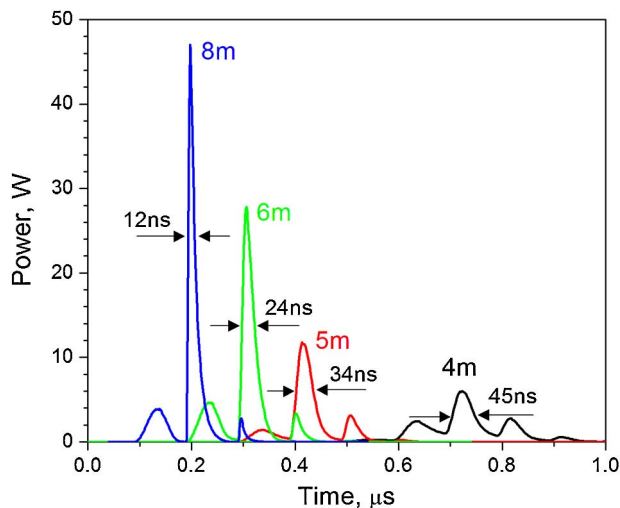

Fig. 4. (Color online) Shapes of QS pulses as a function of the EDF length; EDF lengths are indicated near the correspondent curves. All curves are simulated for the laser output 1; see Fig. 2. The cavity length is equal to the experimental value (10.3 m). The zero-time corresponds to the moment of the AOM switching on.
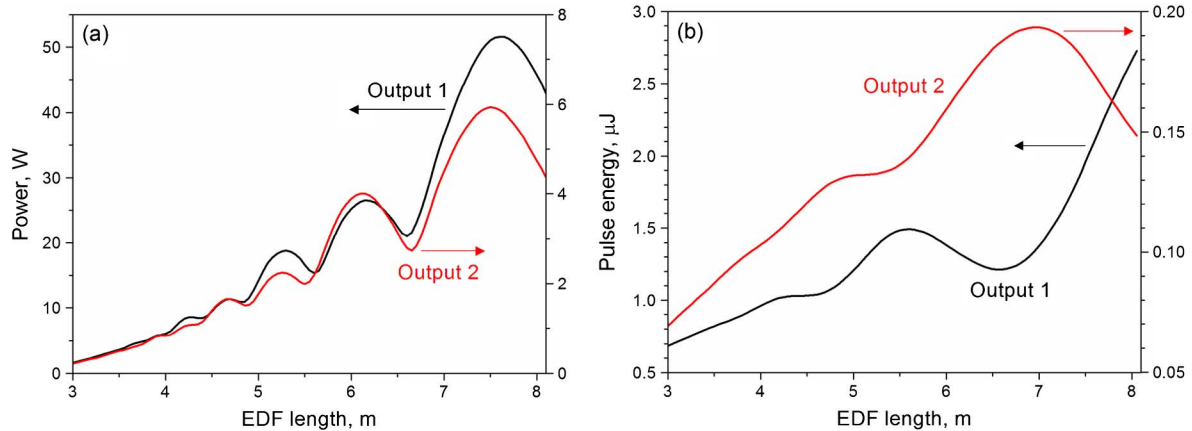
Fig. 5.   (Color online) Theoretical dependence of (a) the main subpulse peak power and (b) the pulse energy, both on EDF length. The curves are labeled by the correspondent laser output number.

implementation is the symmetric one discussed in the next section.

B. Symmetric Laser Configuration

A QS-EDFL in symmetric configuration was modeled in a similar way. In this case, the AOM was considered to be placed exactly at the center of the cavity, thus dividing the EDF into two equal sections (EDF1 and EDF2; see Fig. 3); each EDF section was considered to be pumped separately.

At the beginning of a QS pulse's formation, the AOM is blocked ($t \leq 0$), so SE born and amplified in each EDF section does not propagate into another section. When the AOM starts switching on, ASE begins to be amplified by the other EDF piece, hence forming two contrapropagating signal (laser) waves whose optical spectrum is determined by the reflection bandwidths of the FBG reflectors. After consecutive amplifications by the EDF pieces and reflections by the FBG couplers, these waves form the output QS pulses leaving from the two laser outputs. Since each even subpulse in a QS pulse is formed by one of two contrapropagating signal waves and each odd subpulse is formed by another signal wave, the adjacent subpulses on the laser output are separated by the interval that approximately correspond to one-way trip through the laser cavity.

When modeling, we focused on symmetric configuration of a QS-EDFL with the EDF length varied from 2 to 4 m each. So the total EDF length in this case was measured from 4 to 8 m, the circumstance that can be directly compared with the results obtained when modeling the asymmetric configuration of the laser (Fig. 5). All the laser parameters, including the EDF type and length, the cavity losses, the reflectivity of FBGs, and the AOM function, were considered to be the same as in experiments (see below).

An example of simulated QS pulses is shown in Fig. 6. It is seen that behavior of QS pulses is quite similar to the one obtained when modeling the asymmetric cavity scheme. That is, a QS pulse always contains several subpulses, which is the result of applying the traveling waves' model. Also, once the EDF length increases a QS pulse as whole appears earlier while its main constituent (with the highest power) decreases from 36 ns (EDF: 4 m) to 18 ns (EDF: 8 m). The only difference is that subpulses in snapshots are separated now by 64 ns, the interval that corresponds to the one-way trip through the laser

cavity, not to the round-trip as was observed for the asymmetric cavity configuration.

Notice here that the operation principle of a symmetric-cavity QS-FL is very similar to that of a multipass optical amplifier [24]; a sole difference between these circumstances is that in our case the two contrapropagating seed pulses are formed by the AOM placed inside the cavity.

Figures 7(a) and 7(b) demonstrate the dependences of the main peak power and energy of the whole QS pulse on the overall EDF length. Similarly to the asymmetric cavity configuration, the QS power is seen to grow with the EDF length [Fig. 7(a)]: it is changed at both outputs 1 and 2 from ≈3 W at 3 m (2×1.5 m) length of the EDF to ≈45 W at 8 m (2×4 m) fiber. These dependences have behavior somewhat similar to the ones obtained above for the asymmetric cavity QS-EDFL [compare with Fig. 5(a)]: they present certain local extremes, with the most prominent maximum being observed at the same EDF length of ≈7.6 m. The QS pulse energy [Fig. 7(b)] also increases with an increase of the EDF length, as it does in the case of the QS-EDFL with asymmetric cavity. However, these changes now are "in phase" at the opposite laser outputs, unlike the case of asymmetric cavity [compare with Fig. 5(b)], given by a symmetric position of the AOM
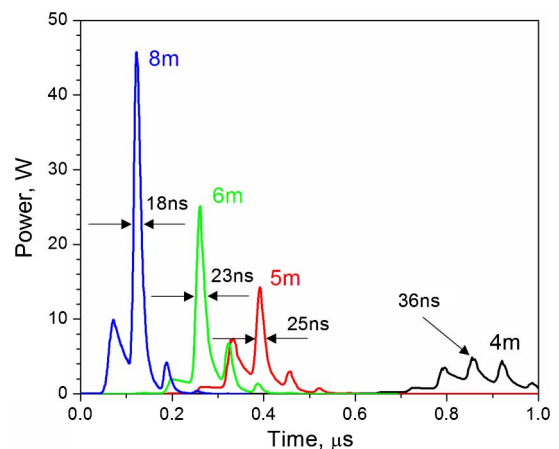

Fig. 6.   (Color online) Total EDF lengths are indicated near the correspondent curves. All curves are simulated for the laser output 1; see Fig. 3. The cavity length is equal to the experimental value (13.4 m). The zero-time corresponds to the moment at which the AOM is switching on.
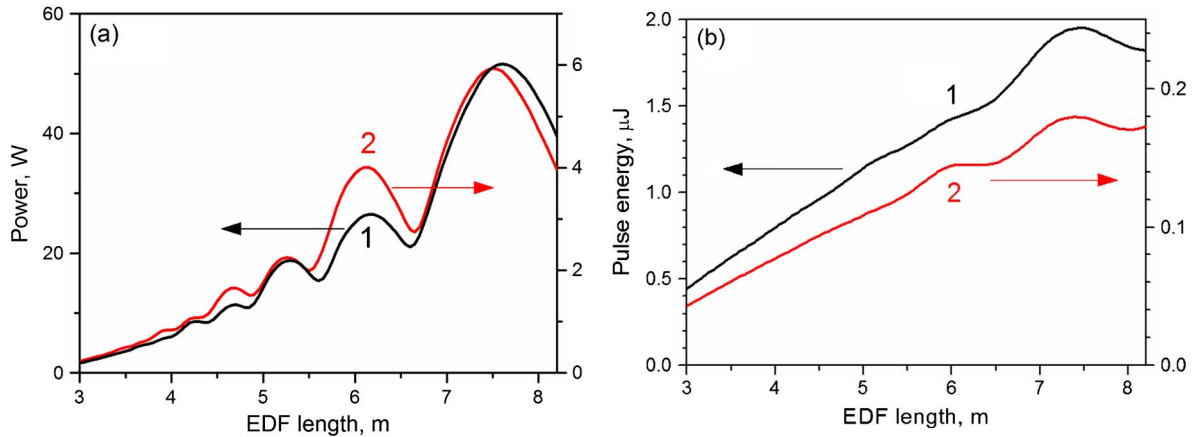
Fig. 7.   (Color online) Theoretical dependence of (a) the main subpulse peak power and (b) the pulse energy, both on EDF length. The curves are labeled by the correspondent laser output number.

relative to the FBG reflectors. [Note that the maximal output energy released from output 1 (≈ 2 μJ at the optimal EDF length, 7.6 m) is by $\approx 50\%$ less than that in the asymmetric implementation of the laser with the same EDF length, which is explained by extra fiber splices on the AOM right side, leading to an increase of the total intracavity cavity loss].

4. EXPERIMENTAL

A. Experimental Setup
Experimental setups of the QS-EDFL with asymmetric and symmetric cavity configurations are sketched in Figs. 2 and 3, respectively. One or two fiber-coupled semiconductor lasers (operation wavelength $\lambda_p \approx 976$ nm) were used for in-core pumping of correspondingly one or two pieces of a standard low-doped EDF (*Thorlabs*, M5-980-125) through $980/1550$ nm wavelength division multiplexers (WDMs). Overall lengths of the cavities in these two cases were $L_c = 10.3$ and 13.4 m, respectively: these included one or two 4 m pieces of the EDF (correspondingly in the asymmetric and symmetric implementations) and also rather long pieces of passive SMF fiber, gathering all the intracavity components together. The reflection coefficients of the FBG1 and FBG2 reflectors were 37% and 93% with spectral bandwidths of ≈ 100 and ≈ 110 pm, respectively. The FBGs were tuned mechanically to adjust their reflection peaks to a wavelength $\lambda_s = 1550$ nm.

We used for QS a fiber-coupled AOM (*Gooch & Housego*, M111-2J-F2S) for the wavelength 1550 nm with a driving acoustical frequency of 111 MHz. When AC voltage at this frequency was applied to the AOM, a collimated input beam was switched between the zero and the first diffraction orders, the latter being the AOM output. The AOM transmission in the open ("on") state was 38%, which corresponds to the transmission loss of ≈ 4.2 dB. The AOM switching function was registered prior to the main-course experiments, which is described by Eq. [6] (see Section 2). The AOM transparency window was chosen to be 5 μs.

The laser signals were registered by a photo-receiver (*New Focus*, DC to 125 MHz) connected to a 400 MHz digital oscilloscope. Each EDF piece was in-core pumped at $P_{p0} = 200$ mW at the points z_1 and z_4 (see Fig. 3). The AOM repetition rate was chosen to be comparatively low ($f_m = 100$ Hz), which provides a maximized population inversion level in the

EDF prior the AOM is switching on. This allowed us to ensure that maximal energies and peak powers of QS pulses are extracted from the laser system.

B. Experimental Results and Discussion
We experimented with the QS-EDFL assembled in both asymmetric and symmetric configurations, modeling of which was performed in Sections 2 and 3.

Figure 8 demonstrates the oscilloscope traces of QS pulses recorded from both laser outputs 1 and 2 (circles) and also the correspondent ones obtained from the modeling (solid curves).

It is seen that the model fits the shape of experimental pulses even in details. For instance, QS pulses contain several subpulses (six and three subpulses for the asymmetric and symmetric cavity configurations, respectively). In the case of asymmetric cavity, subpulses are separated by ≈ 100 ns, which approximately equals the round-trip time of light through the cavity, and are "out of phase" when detected at the cavity opposite sides. In the case of symmetrical cavity, subpulses are less separated (by ≈ 67 ns, the time interval that corresponds to the one-way trip of light through the cavity, not to the round-trip as in the previous case). The total energy and peak power of QS pulses, measured at output 1 in the symmetric configuration, is ≈ 1.8 μJ and ≈ 48 W, respectively (thus being by correspondingly $\approx 40\%$ and ≈ 8 dB higher as compared with the results of simulation of the asymmetric configuration).

Slight differences seen in Fig. 8 between the experiments and modeling data can arise due to the following factors: (i) The model does not take into account the radial intensity distribution of the fiber fundamental mode; hence, radial non-uniformities in the populations of Er^{3+} levels [25] are ignored. This would result in some over- or underestimating of the EDF gain, which, in turn, would lead to errors in the calculated values of intracavity laser power and in the decay rate of the laser level. (ii) The model ignores the laser spectrum's narrowing that takes place at each reflection of light by the FBGs. This effect may also retard the laser level decay.

Let's discuss in more detail the symmetric configuration, referring to the black left snapshots in Fig. 8. One can reveal from the modeling results that the first subpulse (marked 1a in the figure) in the QS pulse, which appears on the left side of the second (main) one (1b), is the ASE portion that is initially
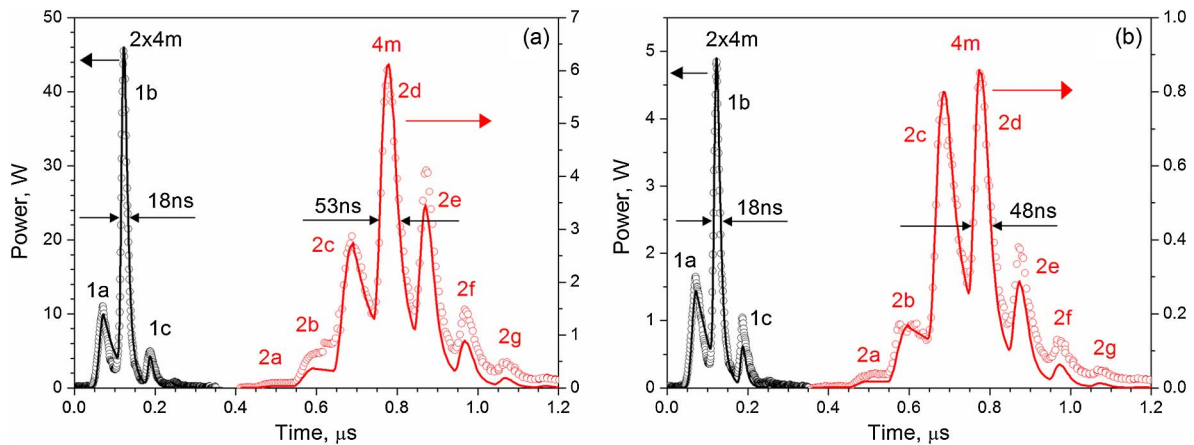
Fig. 8.   (Color online) Theoretical (solid curves) and experimental (circles) shapes of SQ-EDFL output pulse measured from (a) output 1 and (b) output 2. The left graphs (marked as 2×4 m) correspond to the symmetric QS-EDFL, and the right graphs (marked as 4 m), to the asymmetric QS-EDFL. Zero-times correspond to the moments of switching the AOM on. The main pulses are labeled as 1b and 2d in the symmetric and asymmetric configurations, respectively.

created in one of the EDF pieces, when the AOM is off ($t < 0$) and then propagates along the cavity 1.5 times. Due to the relatively high intracavity loss (approximately 8 dB for one trip along the cavity) and a small number of travels of light along the cavity, this subpulse is not that powerful to depopulate the Er^{3+} laser level $^4I_{13/2}$. The next (and the biggest) subpulse (1b) is created in another EDF piece (remind that the AOM is off) and then propagates along the cavity 2.5 times. Since this subpulse survives within the EDF for a longer time, it is more effectively amplified and becomes very intense. It is also worth noticing that this subpulse, during the last pass through the cavity, strongly depopulates the laser level, thus dropping the EDF gain down to negative values. At last, the third subpulse (1c) passes along the cavity 3.5 times, with the last path being made when the EDF is already absorbing (see above). Therefore its magnitude becomes the smallest. All other subpulses that propagate through the cavity for 0.5 or 4.5, 5.5, and more times are too small in magnitude to be registered.

An interesting effect observed experimentally and found in the modeling is that some "squeezing" is observed in the time domain of subpulses' separation respective to the tentatively expected one, given by simple estimates for the time needed for light to propagate the laser cavity. Though the round-trip time, in the case of 13.4 m symmetric cavity, is estimated to be ≈130 ns, a real subpulse separation (measured experimentally and given by the modeling) is by 11–13% less. For instance, the first (1a) and the third (1c) subpulses that are formed by the same signal wave are separated by only ≈116 ns. The "effective" cavity length found from the last value is ≈11.9 m instead of ≈13.4 m of its physical value. Such an effect can originate from strong amplifying of the front-edge of a subpulse within the still "charged" EDF and also from strong absorbing of its trail-edge within an already "discharged" EDF. A similar process has been observed recently in saturated EDF amplifiers for unshaped input pulses; see, e.g., Fig. 2(b) in [26] and Fig. 3(b) in [27].

As about the asymmetrical configuration (refer to the red right snapshots in Fig. 8), the first subpulse (2a) appears after 4.5 or 5.5 one-way trips through the cavity, depending on which of the laser outputs (1 or 2) is under test. The QS pulses as whole consist of seven subpulses in this case, so the peak

power is much less, while the pulsewidth is much bigger than in the symmetric configuration.

Thus, we can conclude that a QS-EDFL implemented in the symmetric cavity configuration allows one to obtain QS pulses with substantially improved temporal and energetic characteristics as compared with such a laser with a standard asymmetric cavity.

5. CONCLUSIONS

In this paper, a QS-EDFL with a symmetric cavity is proposed and discussed in detail. In this laser, a QS AOM is placed exactly at the center of the cavity formed by two FBGs, thus dividing the active EDF into two sections of the same length. This novel scheme for the QS-EDFL is compared with the conventional asymmetric one in which the AOM is placed near one of the FBG's couplers.

Modeling of the QS-EDFL in these two cavity configurations is performed by applying the traveling waves' method, which permits one to explain almost all the features of the QS regime, including the multipeak structure, the shape and duration of QS pulses, and their delay with respect to the moments of the AOM switching on and shortening of intervals between subpulses within the multipeak structure. The model takes into account the point intracavity losses produced by fiber splices and intracavity components and the distributed ones such as the EDF background loss and the loss stemming from the ESA transitions inherent in the EDF. Its applicability for an analysis of the QS-EDFL implemented experimentally is ensured by incorporating the exact function that describes the switching process in the AOM and using the known parameters of the EDF.

We show theoretically that for increasing the energy and power of QS pulses, one needs to increase the intracavity EDF length. However, as seen from the experiments, the EDF length to be used in the QS-EDFL is limited by arising of spurious CW lasing in intervals between QS pulses when the AOM is blocked, given by the presence of internal reflections from the AOM input. In the case of a standard asymmetric cavity configuration of the QS-EDFL, this limitation cannot be overcome at all. However, as our present research showed, there is a unique cavity geometry of the QS-EDFL, the symmetric one,

that allows one to increase the EDF length almost twice (and so to increase the energy and power of QS generated yet without spurious CW lasing). This particular result as a consequence of the development of an accurate model of a *Q*-switched fiber laser is the main news of the present work.

As deduced from the direct comparison of the experimental data with the results of modeling, the symmetric cavity configuration of the QS-EDFL allows enhancing the temporal and energetic parameters of QS pulses. That is, this implementation of the QS-EDFL provides a very stable generation regime of short QS pulses, where the main subpulses (within their multipeak structure) are measured by only 18 ns on a 3 dB level while side subpulses are essentially reduced in magnitude, as compared with the asymmetric cavity configuration. Furthermore, the peak power of the main subpulses obtained using the symmetrical configuration is 8 dB higher and the pulse energy is 40% more than that for the asymmetric cavity configuration. It is interesting but well understandable that for the symmetric cavity the time intervals between subpulses of QS pulses correspond to approximately one-way pass of light between the reflectors in contrast to the case of the asymmetric cavity where subpulses are separated by the time intervals corresponding to an approximately round-trip pass.

The last but not the least is that the modeling results are in excellent agreement with the experimental data, ensuring correctness of the theory and its applicability for further optimization of QS-EDFLs and other fiber lasers with long cavities oscillating in a QS regime.

ACKNOWLEDGMENTS

REFERENCES

1. Y. Okamoto, R. Kitada, Y. Uno, and H. Doi, "Cutting of solid type molded composite materials by *Q*-switched fiber laser with high-performance nozzle," J. Adv. Mech. Design Syst. Manufacturing **2**, 651–660 (2008).
2. W. Shi, M. Leigh, J. Zong, and S. Jiang, "Single-frequency terahertz source pumped by *Q*-switched fiber lasers based on difference-frequency generation in GaSe crystal," Opt. Lett. **32**, 949–951 (2007).
3. W. Shi, M. A. Leigh, J. Zong, Z. Yao, D. T. Nguyen, A. Chavez-Pirson, and N. Peyghambarian, "High-power all-fiber-based narrow-linewidth single-mode fiber laser pulses in the *C*-band and frequency conversion to THz generation," IEEE J. Sel. Top. Quantum Electron. **15**, 377–384 (2009).
4. J. M. Dudley, G. Genty, and S. Coen, "Supercontinuum generation in photonic crystal fiber," Rev. Mod. Phys. **78**, 1135–1184 (2006).
5. A. Roy, M. Laroche, P. Roy, P. Leproux, and J.-L. Auguste, "*Q*-switched Yb-doped nonlinear microstructured fiber laser for the emission of broadband spectrum," Opt. Lett. **32**, 3299–3301 (2007).
6. J. Cascante-Vindas, A. Diez, J. L. Cruz, and M. V. Andres, "Supercontinuum *Q*-switched Yb fiber laser using an intracavity microstructured fiber," Opt. Lett. **34**, 3628–3630 (2009).
7. S. Adachi and Y. Koyamada, "Analysis and design of *Q*-switched erbium-doped fiber laser and their application to OTDR," J. Lightwave Technol. **20**, 1506–1511 (2002).
8. C. Cuadrado-Laborde, P. Perez-Millan, M. V. Andres, A. Diez, J. L. Cruz, and Y. O. Barmenkov, "Transform-limited pulses generated by an actively *Q*-switched distributed fiber laser," Opt. Lett. **33**, 2590–2592 (2008).
9. R. J. De Young and N. P. Barnes, "Profiling atmospheric water vapor using a fiber laser lidar system," Appl. Opt. **49**, 562–567 (2010).
10. J. Tauer, H. Kofler, and E. Wintner, "Laser-initiated ignition," Laser Photon. Rev. **4**, 99–122 (2010).
11. P. Myslinski, J. Chrostowski, J. A. K. Koningstein, and J. R. Simpson, "Self-mode locking in a *Q*-switched erbium-doped fiber laser," Appl. Opt. **32**, 286–290 (1993).
12. P. Roy and D. Pagnoux, "Analysis and optimization of a *Q*-switched erbium doped fiber laser working with a short rise time modulator," Opt. Fiber Technol. **2**, 235–240 (1996).
13. Y. Wang and C. Q. Xu, "Understanding multipeak phenomena in actively *Q*-switched fiber lasers," Opt. Lett. **29**, 1060–1062 (2004).
14. S. A. Kolpakov, Y. O. Barmenkov, A. D. Guzman-Chavez, A. V. Kir'yanov, J. L. Cruz, A. Díez, and M. V. Andrés, "Distributed model for actively *Q*-switched erbium-doped fiber lasers," IEEE J. Quantum Electron. **47**, 928–934 (2011).
15. J. M. Saucedo-Solorio, A. N. Pisarchik, A. V. Kir'yanov, and V. Aboites, "Generalized multistability in a fiber laser with modulated losses," J. Opt. Soc. Am. B **20**, 490–496 (2003).
16. D. J. Richardson, J. Nilsson, and W. A. Clarkson, "High power fiber lasers: current status and future perspectives [Invited]," J. Opt. Soc. Am. B **27**, B63–B92 (2010).
17. A. D. Guzman-Chavez, Y. O. Barmenkov, and A. V. Kir'yanov, "Spectral dependence of the excited-state absorption of erbium in silica fiber within the 1.48–1.59 μm range," Appl. Phys. Lett. **92**, 191111 (2008).
18. Y. O. Barmenkov, A. V. Kir'yanov, A. D. Guzman-Chavez, J. L. Cruz, and M. V. Andres, "Excited-state absorption in erbium-doped silica fiber with simultaneous excitation at 977 and 1531 nm," J. Appl. Phys. **106**, 083108 (2009).
19. M. J. F. Digonnet, ed., *Rare-Earth-Doped Fiber Lasers and Amplifiers*, 2nd ed. (Dekker, 2001), Chaps. 2 and 7.
20. A. V. Kir'yanov and Yu. O. Barmenkov, "Excited-state absorption and ion pairs as sources of nonlinear losses in heavily doped erbium silica fiber and erbium fiber laser," Opt. Express **13**, 8498–8507 (2005).
21. E. Desurvire, *Erbium-Doped Fiber Amplifiers* (Wiley, 1994), Chap. 1.
22. W. L. Barnes, R. I. Laming, E. J. Tarbox, and R. R. Morkel, "Absorption and emission cross-section of Er^{3+} doped silica fibers," IEEE J. Quantum Electron. **27**, 1004–1010 (1991).
23. D. Marcuse, "Loss analysis in single-mode fiber splices," Bell Syst. Tech. J. **56**, 703–718 (1977).
24. R. Xin and J. D. Zuegel, "Amplifying nanosecond optical pulses at 1053 nm with an all-fiber regenerative amplifier," Opt. Lett. **36**, 2605–2607 (2011).
25. J. del Valle-Hernandez, Y. O. Barmenkov, S. A. Kolpakov, J. L. Cruz, and M. V. Andres, "A distributed model for continuous-wave erbium-doped fiber laser," Opt. Commun. **284**, 5342–5347 (2011).
26. A. Malinowski, K. T. Vu, K. K. Chen, J. Nilsson, Y. Jeong, S. Alam, D. J. Lin, and D. J. Richardson, "High power pulsed fiber MOPA system incorporating electro-optic modulator based adaptive pulse shaping," Opt. Express **17**, 20927–20937 (2009).
27. D. Nodop, D. Schimpf, J. Limpert, and A. Tünnermann, "Highly dynamic and versatile pulsed fiber amplifier seeded by a super-luminescence diode," Appl. Phys. B **102**, 737–741 (2011).
28. A. Bellemare, "Continuous-wave silica-based erbium-doped fibre lasers," Prog. Quantum Electron. **27**, 211–266 (2003).
29. C. B. Layne, W. H. Lowdermilk, and M. J. Weber, "Nonradiative relaxation of rare-earth ions in silicate laser glass," IEEE J. Quantum Electron. **11**, 798–799 (1975).
30. C. B. Layne, W. H. Lowdermilk, and M. J. Weber, "Multiphonon relaxation of rare-earth ions in oxide glasses," Phys. Rev. B **16**, 10–20 (1977).
31. M. P. Hehlen, N. J. Cockroft, T. R. Gosnell, and A. J. Bruce, "Spectroscopic properties of Er^{3+}- and Yb^{3+}-doped soda-lime silicate and aluminosilicate glasses," Phys. Rev. B **56**, 9302–9318 (1997).